



ELSEVIER

Contents lists available at ScienceDirect

# Ocean Engineering

journal homepage: [www.elsevier.com/locate/oceaneng](http://www.elsevier.com/locate/oceaneng)

## Modeling and control of a novel over-actuated marine floating platform



Kostas Vlachos\*, Evangelos Papadopoulos

Department of Mechanical Engineering, National Technical University of Athens, 15780 Athens, Greece

### ARTICLE INFO

#### Article history:

Received 6 November 2013

Accepted 1 February 2015

#### Keywords:

Marine vehicle control

Dynamic positioning

Over-actuated control

### ABSTRACT

An autonomous dynamic positioning scheme for a novel triangular floating marine platform is developed, that stabilizes its linear and angular velocities as well as its position and orientation. For this platform, the required closed-loop forces and moments are provided by three rotating pump-jets, located at the bottom of three partly submerged cylinders, located at the corners of the platform. With this control configuration, the platform is over-actuated, i.e., it has more control inputs than degrees of freedom (DOF). Design guidelines leading to balanced actuator loading are identified. A control allocation scheme is developed that allows for station keeping under realistic constraints, disturbances and hardware limitations, without violating thruster dynamics. Furthermore, a model-based controller is proposed that aims at the reduction of fuel consumption. Simulation results, in the presence of realistic environmental disturbances, are presented that demonstrate the performance of the controller and of the allocation scheme developed. Preliminary Hardware-In-the-Loop (HIL) real time experiments are conducted and presented, showing effective platform station keeping.

© 2015 Elsevier Ltd. All rights reserved.

### 1. Introduction

Floating platforms are widely used in the offshore petroleum industry, as portable pipeline systems, in-the-field laboratories, etc. (Wilson, 2003). To accomplish their task, these platforms must be kept stationary at a desired position and orientation. Thus, they are equipped with appropriate actuation systems that provide the necessary dynamic positioning to counterbalance the sea waves, wind and current induced forces and moments, and the uncertainties in modeling the platform dynamics (Sørensen, 2011). Floating platform dynamics are inherently nonlinear due to the rigid body dynamics and, more importantly, due to the strong hydrodynamic interactions (Hawary, 2001). Hence, in order to design effective closed-loop controllers, nonlinear techniques are adopted. Control allocation schemes must also be developed; usually, such vessels have redundant actuation, i.e., they have more control inputs than DOF resulting in an over-actuated system. Thus, the closed-loop control forces and moments need to be distributed efficiently to the actuators in such a way that the control objective is realized without violating operational constraints (e.g. thruster capabilities). The issue leads, in general, to a constrained optimization problem that is hard to solve using even

state-of-the-art iterative numerical optimization software in a safety-critical real-time system with limiting processing capacity (Fossen and Johansen, 2006). Nevertheless, real-time iterative optimization solutions have been proposed in Bodson (2002), Webster and Sousa (1999), and Johansen et al. (2004). Optimal thrust allocation for ships has been addressed in Berge and Fossen (1997). To address a related problem, i.e. the positioning of large surface vessels using multiple tugboats, an adaptive position controller has been proposed in Braganza et al. (2007). However in this work, the tugboat dynamics and the environmental disturbances are not taken under consideration. In addition, the incident angles of the tugboats are considered to be constant. The same problem was studied in Feemster and Esposito (2011), where an adaptive tracking controller and a force allocation scheme were proposed under actuator saturation, uncertain hydrodynamic parameters, and environmental disturbances. Again, the direction of the thrust of each actuator was considered as fixed and the dynamics of the actuators (tugboats) was not studied.

Thrusters that can be rotated are usually mounted under the hull of the vessel. Optimization schemes for such actuation configurations have been proposed, for example in Sjørdalen (1997). In Lynch (1999), controllability issues regarding the plane motion were studied. The use of a Kalman filter has been proposed for filtering noisy measurements of the ship motion (Fossen and Perez, 2009).

The authors presented early results on marine platform dynamic positioning in Repoulas et al. (2008) and Vlachos and

\* Corresponding author. Tel.: +30 2107722643.

E-mail addresses: [kostaswl@central.ntua.gr](mailto:kostaswl@central.ntua.gr) (K. Vlachos), [egpapado@central.ntua.gr](mailto:egpapado@central.ntua.gr) (E. Papadopoulos).

Papadopoulos (2010). In Repoulas et al. (2008), an initial dynamic model of the floating platform and a simplified control allocation scheme were described, while in Vlachos and Papadopoulos (2010), a controller is presented that neglects the actuator dynamics. These works assumed primitive models of system disturbances.

This work focuses on the development and implementation of an autonomous dynamic positioning scheme for the novel triangular marine platform, shown in Fig. 1. The scheme aims at stabilizing the platform position and orientation under actuator constraints, in the presence of realistic environmental disturbances, and must be implementable in real time.

The platform positioning forces and moments are provided by three rotating pump-jets. The system is over-actuated; hence, a proper control allocation scheme is developed to allow for optimal allocation of the effort without violating thruster capabilities. To improve the overall power efficiency, the developed scheme is designed to minimize the pump-jet thrust activity. To distribute to the jets the required control force and moment in a balanced way, design rules are formulated that minimize the condition number of the normalized transformation matrix relating the control forces and the platform jet thrusts. A model-based controller, aiming at further reduction of the fuel consumption, is described and evaluated.



Fig. 1. The triangular marine platform (under construction).

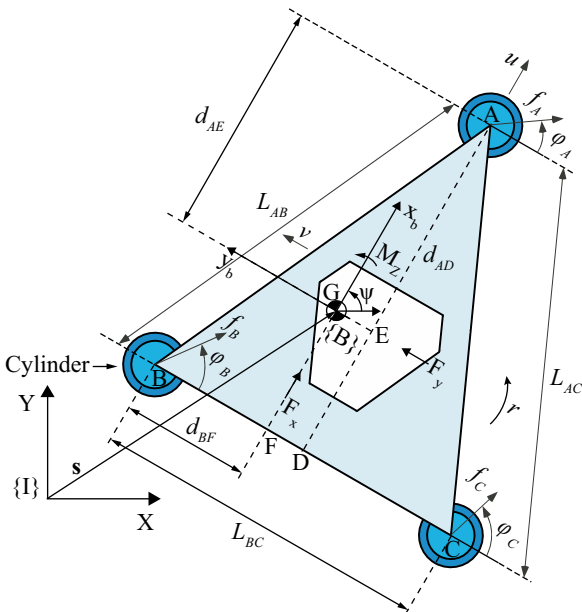


Fig. 2. A 2D representation of the platform.

Compared to the complex, on-line, and iterative algorithms, the developed methodology provides a fast and computationally inexpensive algorithm that drives the platform to a position with prescribed tolerance. Simulation results, including environmental disturbances such as sea currents, wind generated waves, and wind forces, validate the performance of the controller and its allocation scheme. Additionally, preliminary Hardware-In-the-Loop (HIL) real time experiments are conducted and discussed.

### 1.1. General description

The platform “DELTA VERENIKI”, currently under construction, see Fig. 1, is designed to assist in the deployment of the deep-sea cubic kilometer neutrino telescope “NESTOR” ([www.nestor.noa.gr](http://www.nestor.noa.gr)). The platform consists of a triangular structure mounted on three hollow double-cylinders, one at each corner of the structure. The plane of the triangle is parallel to the sea surface. The cylinders provide the necessary buoyancy, as part of them is immersed in the water. The platform actuation is realized using three fully submerged pump-jets, located at the bottom of each cylinder. Diesel engines drive the pumps, while electro-hydraulic motors rotate the jets providing vectored thrust.

### 1.2. Geometry and kinematics

The main body of the structure has the shape of an isosceles triangle with side length  $L_{AB}=L_{AC}$  and base length  $L_{BC}$ . The center of mass (CM) of the platform is at point G, see Fig. 2.

To describe the kinematics of plane motion, two reference frames are employed, the inertial reference frame {I} and the body-fixed frame {B}, see Fig. 2. As shown, the origin of {B} frame coincides with the platform CM. The  $x_b$  body-fixed axis is parallel to the platform symmetry axis AD,  $y_b$  is parallel to the shortest triangle side and  $z_b$  points upwards, see Fig. 2. We focus on the platform planar motion; actuation and control along the  $z_b$  axis (heave), and about the  $x_b$  (roll) and  $y_b$  (pitch) axes, are outside the scope of this work. Then, the kinematics equations of the plane motion are described by

$${}^I\dot{\mathbf{x}} = {}^I\mathbf{R}_B {}^B\mathbf{v} \quad (1a)$$

where

$${}^I\dot{\mathbf{x}} = [\dot{x}, \dot{y}, \dot{\psi}]^T \quad (1b)$$

$${}^B\mathbf{v} = [u, v, r]^T \quad (1c)$$

$${}^I\mathbf{R}_B = \begin{bmatrix} c\psi & -s\psi & 0 \\ s\psi & c\psi & 0 \\ 0 & 0 & 1 \end{bmatrix} \quad (1d)$$

with  $s = \sin(\cdot)$ ,  $c = \cos(\cdot)$ . In (1b),  $x$  and  $y$  represent the CM inertial coordinates and  $\psi$  describes the orientation of {B} with respect to {I};  $u$  and  $v$  are the surge and sway velocities respectively, defined in the body-fixed frame {B}, and  $r$  is the yaw (angular) velocity of the platform.

To compute the hydrodynamic forces and moments that are applied by the hydrodynamic interaction of the submerged part of the cylinders and the water, we need to establish the cylinder location in {B}. To this end, we introduce some necessary notation:  ${}^B\mathbf{s}_{A/G}$  is the position of point A with respect to G expressed in {B}, while  ${}^B\mathbf{s}_{B/G}$  and  ${}^B\mathbf{s}_{C/G}$  have similar meanings;  ${}^B\mathbf{v}_{i,i} = [u_i, v_i]^T$  is the linear velocity vector of point  $i$ , where  $i=A, B, C$ ,  ${}^B\mathbf{a}_{i,i} = {}^B(d\mathbf{v}_{i,i}/dt)_i$  is the linear acceleration vector, and  $\alpha = dr/dt$  is the angular acceleration, all expressed in {B}. Then, the following geometric

relations hold:

$${}^B \mathbf{s}_{A/G} = \left[ d_{AE}, d_{BF} - \frac{L_{BC}}{2} \right]^T \quad (2a)$$

$${}^B \mathbf{s}_{B/G} = [- (d_{AD} - d_{AE}), d_{BF}]^T \quad (2b)$$

$${}^B \mathbf{s}_{C/G} = [- (d_{AD} - d_{AE}), d_{BF} - L_{BC}]^T \quad (2c)$$

Velocities and accelerations are given by

$${}^B \mathbf{v}_{I,A} = \left[ u + r \left( \frac{L_{BC}}{2} - d_{BF} \right), v + r d_{AE} \right]^T \quad (3a)$$

$${}^B \mathbf{a}_{I,A} = \left[ \dot{u} - \alpha \left( d_{BF} - \frac{L_{BC}}{2} \right) - r^2 d_{AE}, \dot{v} + \alpha d_{AE} - r^2 \left( d_{BF} - \frac{L_{BC}}{2} \right) \right]^T \quad (3b)$$

$${}^B \mathbf{v}_{I,B} = [u - r d_{BF}, v - r (d_{AD} - d_{AE})]^T \quad (3c)$$

$${}^B \mathbf{a}_{I,B} = [\dot{u} - \alpha d_{BF} + r^2 (d_{AD} - d_{AE}), \dot{v} - \alpha (d_{AD} - d_{AE}) - r^2 d_{BF}]^T \quad (3d)$$

$${}^B \mathbf{v}_{I,C} = [u + r (L_{BC} - d_{BF}), v - r (d_{AD} - d_{AE})]^T \quad (3e)$$

$${}^B \mathbf{a}_{I,C} = [\dot{u} + \alpha (L_{BC} - d_{BF}) + r^2 (d_{AD} - d_{AE}), \dot{v} - \alpha (d_{AD} - d_{AE}) + r^2 (L_{BC} - d_{BF})]^T \quad (3f)$$

### 1.3. Dynamics

In the vertical direction, the structure oscillates because of the change in buoyancy forces: if the structure is submerged more with respect to its equilibrium, the buoyancy is increased pushing the platform upwards, and vice-versa. At equilibrium, the cylinder height  $h$  above the surface is given by

$$h = H_{uc} - (1/R_{uc}^2)((m/3\pi\rho_w) - R_{lc}^2 H_{lc}) \quad (4)$$

where  $\rho_w$  is the water density and  $m$  is the total mass of the platform, and the remaining variables are defined in Fig. 3.

The hydrodynamic forces are due to the motion of the cylinders into the moving water. The hydrodynamic force acting on each cylinder includes three terms. The first term is the added mass force, which is a linear function of the relative acceleration of each cylinder with respect to the acceleration of the water. The second term is the inertia force which is a linear function of the acceleration of the water, while the third term is the drag force, which is a quadratic function of the relative velocity between the water and each cylinder, see Hoerner (1965) and American Petroleum Institute (2000). As an example, the normal to the axis of each cylinder force on the double-cylinder structure at point A,

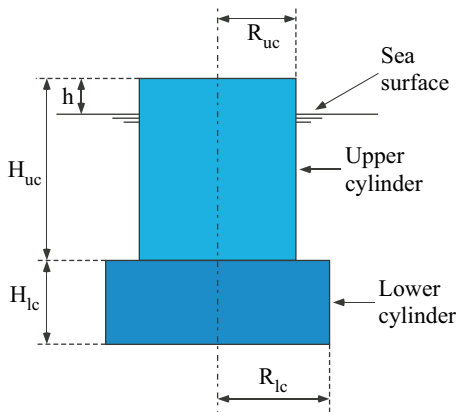


Fig. 3. A side view of the double-cylinder structure.

expressed in body-fixed frame {B}, is given by

$$\begin{aligned} {}^B \mathbf{f}_{h,A} = & C_a \pi \rho_w [R_{uc}^2 (H_{uc} - h) + R_{lc}^2 H_{lc}] \left( \frac{d^B \mathbf{v}_{wat}^\perp}{dt} - {}^B \mathbf{a}_A \right) \\ & + \pi \rho_w [R_{uc}^2 (H_{uc} - h) + R_{lc}^2 H_{lc}] \frac{d^B \mathbf{v}_{wat}^\perp}{dt} \\ & + C_d \rho_w [R_{uc} (H_{uc} - h) + R_{lc} H_{lc}] \|({}^B \mathbf{v}_{wat}^\perp - {}^B \mathbf{v}_A)\| ({}^B \mathbf{v}_{wat}^\perp - {}^B \mathbf{v}_A) \end{aligned} \quad (5a)$$

where  $C_a$  is the added mass coefficient and  $C_d$  the drag coefficient.  ${}^B \mathbf{v}_{wat}^\perp$  is the component of the velocity vector of the water normal to the axis of each cylinder, calculated from the vectorial addition

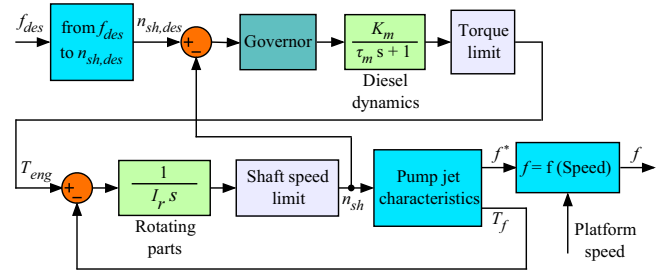


Fig. 4. Actuator thrust,  $f$ , dynamics.

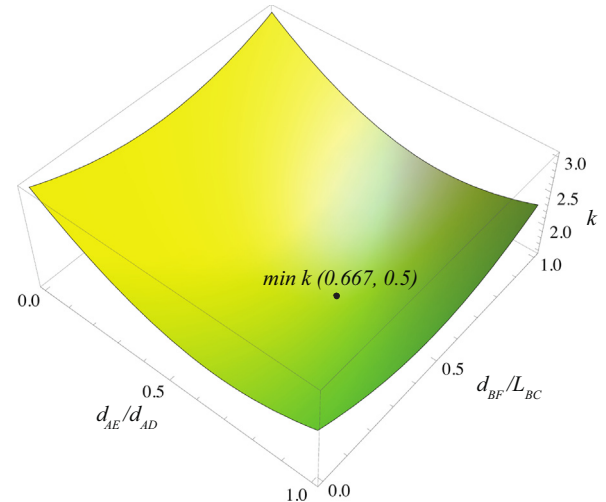


Fig. 5. Condition number  $k$  as a function of the location of the platform's CM.

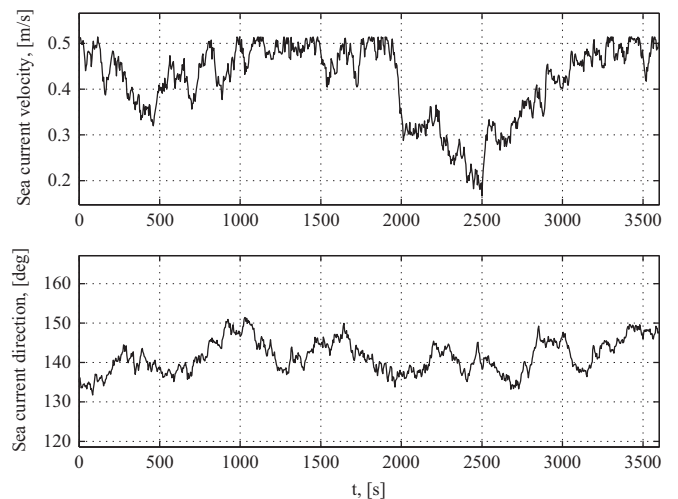


Fig. 6. Sea current velocity and direction.

of the sea current velocity,  ${}^B\mathbf{v}_{cur}$ , and the water flow velocity due to sea waves,  ${}^B\mathbf{v}_{wav}$ , all expressed in the body-fixed frame:

$${}^B\mathbf{v}_{wat}^\perp = ({}^B\mathbf{v}_{cur} + {}^B\mathbf{v}_{wav})^\perp \quad (5b)$$

The hydrodynamic forces on the cylinder A given by (5a) result in a force acting on the platform CM and a moment about it, i.e.

$${}^B\mathbf{q}_{h,A} = [{}^B\mathbf{f}_{h,A}^T, ({}^B\mathbf{s}_{A/G} \times {}^B\mathbf{f}_{h,A})^T]^T \quad (6)$$

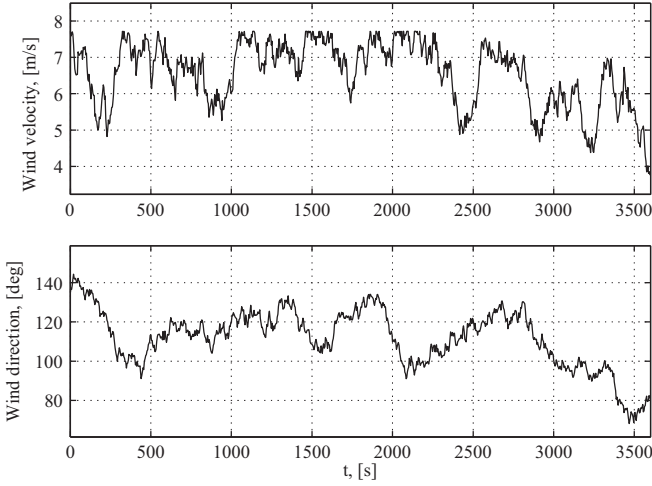


Fig. 7. Wind velocity and direction.

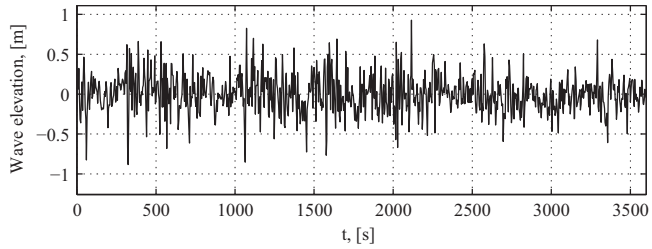


Fig. 8. Wave elevation.

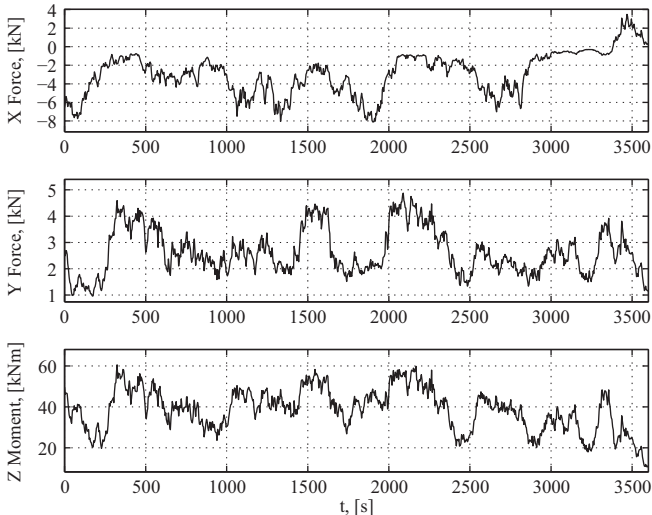


Fig. 9. Wind induced forces and moment on the platform.

As mentioned already, the jets can provide vectored thrust and thus more flexibility in control design.  $f_A$ ,  $f_B$ , and  $f_C$  in Fig. 2 denote the magnitudes of the thrusts while  $\varphi_A$ ,  $\varphi_B$ , and  $\varphi_C$  denote the forces directions. These thrusts provide control forces in  $x_b$  and  $y_b$  axes,  $f_{c,x}$  and  $f_{c,y}$  respectively acting on the CM, and torque  $n_{c,z}$  about  $z_b$ , according to the linear transformation:

$${}^B\mathbf{q}_c = [f_{c,x}, f_{c,y}, n_{c,z}]^T = \mathbf{J}^B \mathbf{f}_c \quad (7a)$$

where  ${}^B\mathbf{q}_c$  is the control force/torque vector and

$$\mathbf{J} = \begin{bmatrix} 1 & 0 & -(d_{BF} - (L_{BC}/2)) \\ 0 & -1 & -d_{AE} \\ 1 & 0 & -d_{BF} \\ 0 & -1 & (d_{AD} - d_{AE}) \\ 1 & 0 & (L_{BC} - d_{BF}) \\ 0 & -1 & (d_{AD} - d_{AE}) \end{bmatrix}^T \quad (7b)$$

$${}^B\mathbf{f}_c = [f_A s \varphi_A, f_A c \varphi_A, f_B s \varphi_B, f_B c \varphi_B, f_C s \varphi_C, f_C c \varphi_C]^T \quad (7c)$$

The drag terms and the terms that are functions of the derivative of  ${}^B\mathbf{v}_{wat}^\perp$  in (5a) are collected together and their sum defines the vector  ${}^B\mathbf{q}_{wat}$  i.e., a vector which depends on water speed and acceleration, and has the form

$${}^B\mathbf{q}_{wat} = [f_{x,wat}, f_{y,wat}, n_{z,wat}]^T \quad (8a)$$

Similarly, all terms that are a quadratic function of the rotational velocity of the platform are collected in vector  ${}^B\mathbf{q}$ , given by

$${}^B\mathbf{q} = \begin{bmatrix} m_a(2d_{AD} - 3d_{AE})r^2 \\ m_a((3/2)L_{BC} - 3d_{BF})r^2 \\ 0 \end{bmatrix} \quad (8b)$$

$$m_a = -C_a \pi \rho [R_{uc}^2 (H_{uc} + R_{ic}^2 H_{ic})] \quad (8b)$$

where  $m_a$  is the coefficient of the relative platform acceleration in (5a). We also define the disturbance vector  ${}^B\mathbf{q}_{dist}$ , given by

$${}^B\mathbf{q}_{dist} = {}^B\mathbf{q}_{wind} + {}^B\mathbf{q}_{wat} \quad (8c)$$

where the term  ${}^B\mathbf{q}_{wind}$  represents wind generated disturbance forces and torques (additional information is given in Section 3) and has the form

$${}^B\mathbf{q}_{wind} = [f_{x,wind}, f_{y,wind}, n_{z,wind}]^T \quad (8d)$$

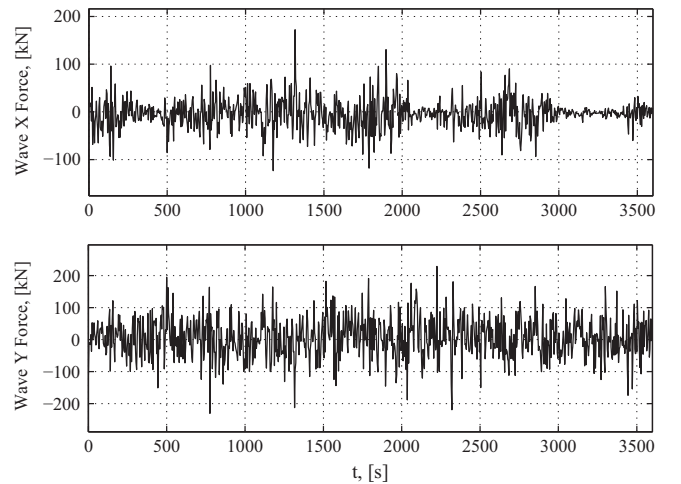


Fig. 10. Wave induced forces on each cylinder.

**Table 1**  
System data and initial conditions.

Parameter	Symbol	Value
Start position in X axis	$x_s$	5.00 m
Start position in Y axis	$y_s$	5.00 m
Start direction	$\psi_s$	10.00°
Start surge velocity	$u_s$	0.10 m/s
Start sway velocity	$v_s$	-0.10 m/s
Start yaw velocity	$r_s$	0.01 rad/s
Total mass of the structure	$m$	425,000.00 kg
Length of the triangular structure side	$L_{AB}$	45.00 m
Length of the triangular structure base	$L_{BC}$	35.00 m
Distance of CM from vertex A	$d_{AE}$	27.64 m
Distance of CM from vertex E	$d_{CE}$	0.00 m
Radius of the upper cylinder	$R_{uc}$	2.20 m
Radius of the lower cylinder	$R_{lc}$	3.50 m
Height of the upper cylinder	$H_{uc}$	6.50 m
Height of the lower cylinder	$H_{lc}$	3.00 m
Jet maximum rotation speed	$\dot{\varphi}_{q, max}$	0.84 rad/s
Jet rotation time constant	$\tau_\varphi$	1.00 s
Diesel engine thrust time constant	$\tau_d$	0.25 s
Diesel engine maximum torque	$T_{eng, max}$	1323.00 Nm
Maximum shaft speed	$n_{sh, max}$	1600.00 rpm
Minimum shaft speed	$n_{sh, min}$	400.00 rpm
Inertia of the pump-jet rotating parts	$I_r$	150.00 kg m <sup>2</sup>
Added mass coefficient	$C_a$	0.80
Drag coefficient	$C_d$	0.80
Air density	$\rho$	1.22 kg/m <sup>3</sup>
Sea water density	$\rho_w$	1024.00 kg/m <sup>3</sup>

Using the above preliminaries, we derive the equations of motion of the platform in plane motion, in {B}:

$$\mathbf{M}^B \dot{\mathbf{v}} = {}^B \mathbf{q} + {}^B \mathbf{q}_{dist} + {}^B \mathbf{q}_c \quad (8e)$$

where  $\mathbf{M} = [m_{ij}]$  is a  $3 \times 3$  mass and added mass matrix, with

$$m_{11} = m_{22} = m - 3m_a$$

$$m_{12} = m_{21} = 0$$

$$m_{13} = m_{31} = 3 \left( d_{BF} - \frac{L_{BC}}{2} \right) m_a$$

$$m_{23} = m_{32} = (2d_{AD} - 3d_{AE}) m_a$$

$$m_{33} = I_{zz} + m_a (-2d_{AD} + 4d_{AD}d_{AE} - 3d_{AE}^2 - (5/4)L_{BC}^2 + 3L_{BC}d_{BF} - 3d_{BF}^2) \quad (8f)$$

where  $I_{zz}$  is the mass moment of inertia about the  $z_b$  axis. It is interesting to point out here that the mass and added mass matrix,  $\mathbf{M}$ , and the vector  ${}^B \mathbf{q}$  become diagonal and zero respectively, simplifying the control structure, if

$$d_{BF}/L_{BC} = 1/2, \quad d_{AE}/d_{AD} = 2/3 \quad (9)$$

i.e. if the CM of the platform is at the triangle's centroid.

#### 1.4. Actuator dynamics and constraints

The azimuth jets that rotate in order to achieve the desired direction of the thrust produce the control force/torque vector  ${}^B \mathbf{q}_c$ . Note that since the thrusters are powered by diesel engines, they cannot produce a negative thrust by changing the direction of rotation of the impeller. Instead, the use of rotating (azimuth) jets implements the change of the thrust direction. However, the desired jet thrust and direction cannot be applied immediately due to actuator dynamics and limitations. In this paper we build the dynamic model of the actuator taking under consideration: (a) the jet rotation dynamics and bounds, and (b) the dynamic characteristics and bounds of the thrust.

To this end, the jet rotation dynamics are modeled as a first order lag according to

$$\dot{\varphi}_q = \frac{1}{\tau_\varphi} (\varphi_{q, des} - \varphi_q) \quad (10)$$

where  $\tau_\varphi$  is the jet rotation time constant. In addition, the rotation speed  $(d\varphi/dt)_q$  is limited by the upper bound  $(d\varphi/dt)_{q, max}$ . The thrust model is more complex and is presented in Fig. 4, in block diagram form. It includes, a number of important dynamics characteristics and limitations such as: (a) the dynamics of the diesel engine, (b) the diesel engine maximum torque  $T_{eng, max}$ , and (c) the maximum shaft speed limit  $n_{sh, max}$ .

In Fig. 4,  $\tau_m$  and  $K_m$  represent the diesel engine time constant and gain respectively,  $T_{eng}$  is the diesel engine torque,  $I_r$  is the inertia of the rotating parts,  $n_{sh}$  is the shaft speed,  $T_f$  is the friction torque, proportional to the shaft speed,  $f$  is the developed pump-jet propulsion force,  $f_{des}$  is the desired pump-jet propulsion force, and  $n_{sh, des}$  represents the desired shaft speed. The torque and shaft speed limits are taken from system specifications. The block entitled "Pump-jet characteristics" describes (i) the relationship between shaft speed and produced force, and (ii) the friction torque,  $T_f$ , as a function of the shaft speed, according to the relevant system data sheets. Likewise, the block entitled "from  $f_{des}$  to  $n_{des}$ " describes the relationship between desired force and shaft speed according to data sheets. As shown in Fig. 4, the propulsion produced by each pump-jet is a function of the platform speed. The block " $f = f(\text{Speed})$ " represents this relationship according to jet specifications, see Schottel (2000) and Caterpillar (2007).

## 2. Design issues

As described by (7b), the jet thrusts produce a platform control force/torque vector via matrix  $\mathbf{J}$ . For control purposes, it is desired that the required control force and moment are resolved to each jet as efficiently as possible. Thus, we examine  $\mathbf{J}$  in order to find under what conditions, this may be possible. Since  $\mathbf{J}$  depends only on platform geometry, the analysis can lead into useful design guidelines. Due to the hydrodynamic forces and other practical constraints, the shape and the overall size of the platform are predetermined. Nevertheless, the location of the platform center of mass  $G$  can be adjusted to some extent by design. To make the analysis insensitive to size or units, (7a) is written as

$${}^B \mathbf{q}_c^* = \mathbf{J}^* {}^B \mathbf{f}_c \quad (11a)$$

where  ${}^B \mathbf{q}_c^*$ ,  $\mathbf{J}^*$ , and  $d_V$  are given by

$${}^B \mathbf{q}_c^* = [f_{c,x}, f_{c,y}, n_{c,z}/d_V]^T \quad (11b)$$

$$\mathbf{J}^* = \begin{bmatrix} 1 & 0 & -(d_{BF} - (L_{BC}/2))/d_V \\ 0 & -1 & -d_{AE}/d_V \\ 1 & 0 & -d_{BF}/d_V \\ 0 & -1 & (d_{AD} - d_{AE})/d_V \\ 1 & 0 & (L_{BC} - d_{BF})/d_V \\ 0 & -1 & (d_{AD} - d_{AE})/d_V \end{bmatrix}^T \quad (11c)$$

$$d_V = (L_{AD} + L_{BC})/2 \quad (11d)$$

The normalized matrix  $\mathbf{J}^*$  has no units and maps the elements of the propulsion vector  ${}^B \mathbf{f}_c$  into the elements of the force vector  ${}^B \mathbf{q}_c^*$ . The propulsion vector  ${}^B \mathbf{f}_c$  is calculated so as to minimize its norm, according to

$${}^B \mathbf{f}_c = \mathbf{J}^{*+} {}^B \mathbf{q}_c^* \quad (12)$$

where  $\mathbf{J}^{*+} = \mathbf{J}^{*T}(\mathbf{J}^* \mathbf{J}^{*T})^{-1}$  is the pseudo-inverse of matrix  $\mathbf{J}^*$ . In using (12), one must also examine the condition number  $k$  of matrix  $\mathbf{J}^* \mathbf{J}^{*T}$ , i.e. the ratio between the highest to the lowest singular value.

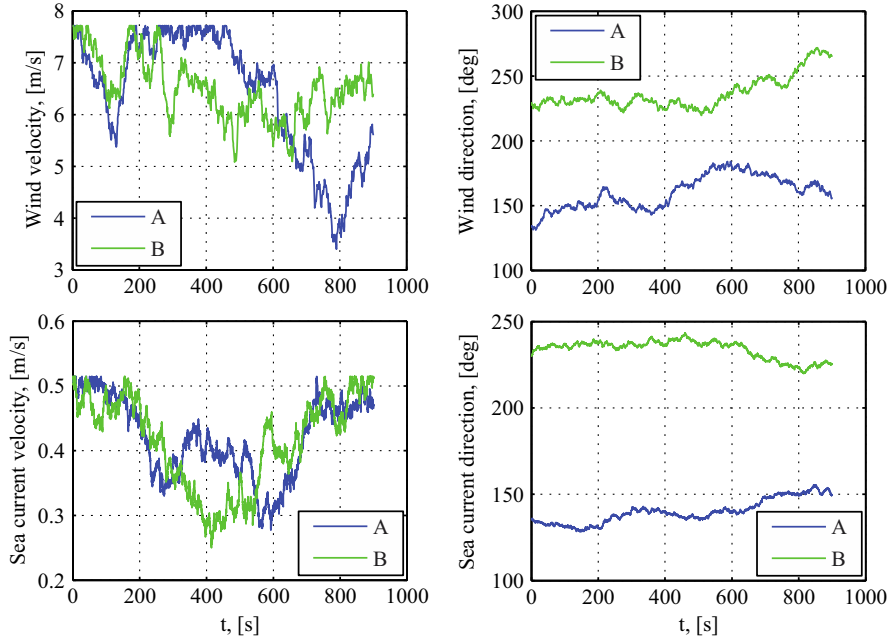


Fig. 11. Environmental disturbances used in simulations for the selection of  $\omega_n$ .

**Table 2**  
Parameters and limits for the simulation of the environmental disturbances.

Parameter	Current velocity	Current direction	Wind velocity	Wind direction
Initial value (A/B)	1/1 kn	135°/230°	15/15 kn	135°/230°
Upper limit	1 kn	360°	15 kn	360°
Lower limit	0 kn	0°	0 kn	0°
Noise mean value	0	0	0	0
Noise variance	0.001	1	0.04	1
Initial seed	Random	Random	Random	Random
Sample time	0.2 s	0.2 s	0.2 s	0.2 s

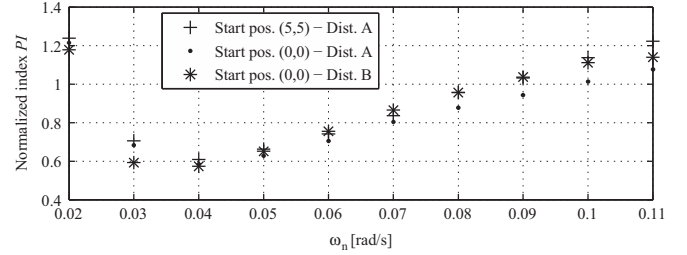


Fig. 13. The normalized performance index PI, for  $0.02 \leq \omega_n \leq 0.11$ .

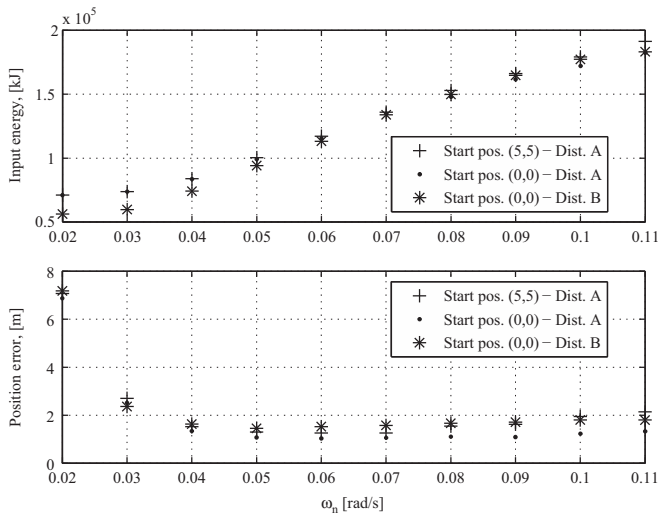


Fig. 12. The average energy consumption of the three jets and the average position error, for  $0.02 \leq \omega_n \leq 0.11$ .

This is because the value of  $k$  represents a measure of the sensitivity of the solution in (12). Hence, our aim is to keep  $k$  as low as possible, ideally close to 1. Using (11c), the singular values

of matrix  $\mathbf{J}^* \mathbf{J}^{*T}$  are found to be

$$\sigma_{1,3} = \frac{\sqrt{N \mp \sqrt{K}}}{2d_V \sqrt{2}}, \quad \sigma_2 = \sqrt{3} \quad (13a)$$

$$N = 11d_{AD}^2 - 16d_{AD}d_{AE} + 12d_{AE}^2 + 6d_{AD}d_{BC} + 8d_{BC}^2 - 12d_{BC}d_{BF} + 12d_{BF}^2$$

$$K = (N)^2 - 8(d_{AD} + d_{BC})^2(4d_{AD}^2 + 3d_{BC}^2) \quad (13b)$$

Since the extensive search of the singular values shows that the inequality  $\sigma_3 \geq \sigma_2 > \sigma_1$  is always true, the condition number  $k$  of matrix  $\mathbf{J}^* \mathbf{J}^{*T}$  is equal to  $\sigma_3/\sigma_1$ . Further investigation of  $k$  using reasonable limits ( $40 \text{ m} < L_{AB} < 80 \text{ m}$  and  $20 \text{ m} < L_{BC} < 40 \text{ m}$ ) shows that the condition number  $k$  is minimum and equal to 1.57907, when (a) the ratio  $d_{AE}/d_{AD}$  is equal to  $2/3$  and (b) the ratio  $d_{BF}/L_{BC}$  is equal to  $1/2$ , i.e. when the CM of the platform coincides with the triangle's centroid. This is also consistent with the diagonalization conditions of the mass and added mass matrix  $\mathbf{M}$ , see (9). Fig. 5 illustrates the above conclusion for  $L_{AB} = 45 \text{ m}$  and  $L_{BC} = 35 \text{ m}$ . Therefore, it is beneficial to design the platform such that the CM is located at the triangle's centroid. In the remainder of the paper, we assume that this is the case.

### 3. Environmental disturbances

The platform dynamic positioning scheme must be able to stabilize its coordinates in the presence of wind, wave, and sea

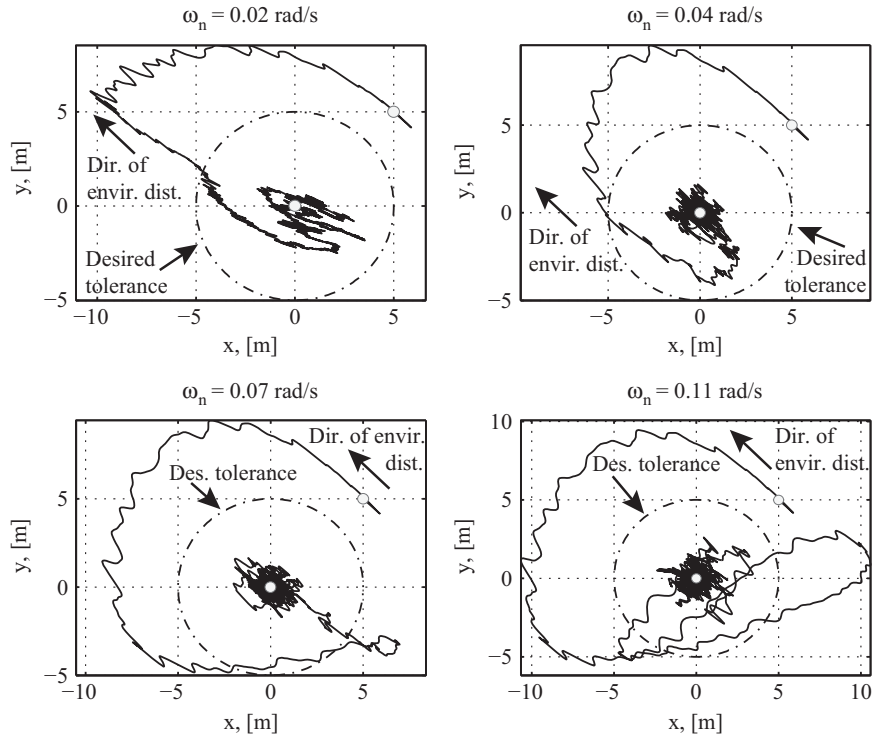


Fig. 14. Platform paths for different  $\omega_n$ .

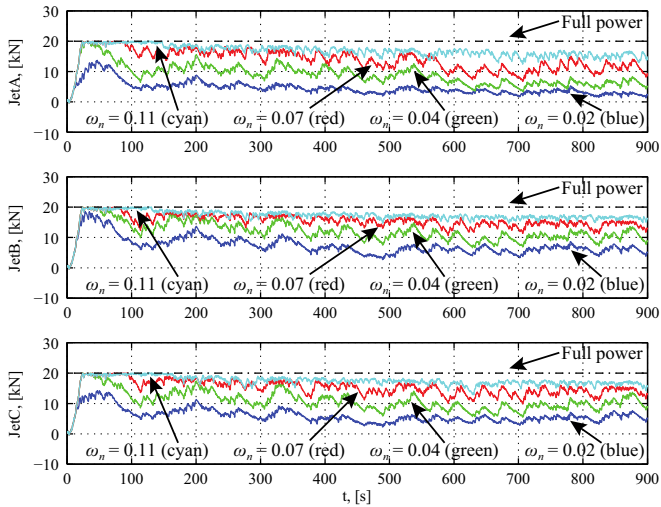


Fig. 15. Jet thrusts for different  $\omega_n$ . (For interpretation of the references to color in this figure, the reader is referred to the web version of this article.)

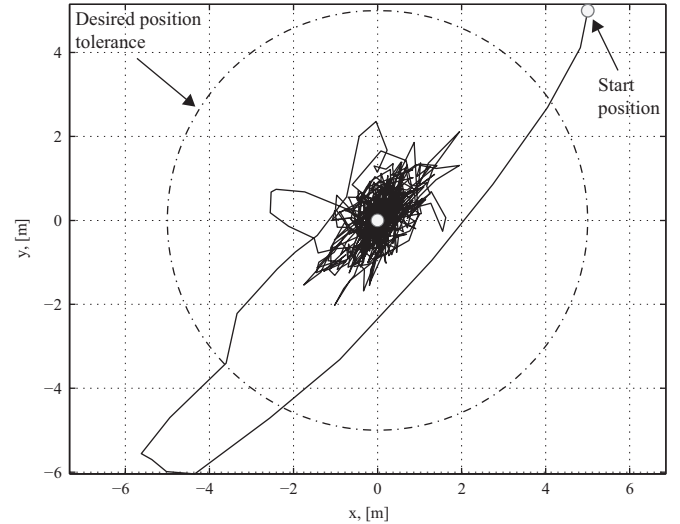


Fig. 16. Dynamic positioning with environmental disturbances.

current environmental disturbances. The models employed to simulate these environmental disturbances are presented here.

The maximum values for the disturbances are defined after analyzing the weather and marine data, collected at the NESTOR site. According to the analysis, almost 50% of the time, the NESTOR site is covered for four consecutive days with winds not exceeding 4 Beaufort. Moreover, the surface current at the NESTOR area has a maximum speed not exceeding 1 kn. Hence, the maximum value of the simulated sea current and wind velocity is 1 kn (0.514 m/s) and 15 kn (7.9 m/s or 4 Beaufort) respectively. Additional information is given at the NESTOR site at [http://www.nestor.noa.gr/NESTOR\\_SITE\\_PROPERTIES/](http://www.nestor.noa.gr/NESTOR_SITE_PROPERTIES/).

The sea current and wave induced forces and moments are included in the dynamic equations of motion by representing (5) in terms of velocity  ${}^B\mathbf{v}_{wat}^+$ , see (5b). The inertial sea current velocity

magnitude and direction used in the simulations are produced by integrating Gaussian white noise. The inertial sea current velocity magnitude,  $v_c(t)$ , is limited such that  $v_c(t) \leq 1$  kn. Fig. 6 presents the corresponding waveforms.

Likewise, the wind velocity magnitude and direction waveforms are produced by integrating white noise. The wind velocity magnitude,  $v_w(t)$ , is limited such that  $v_w(t) \leq 15$  kn (7.9 m/s or 4 Beaufort), see Fig. 7. Fig. 8 demonstrates the wave elevation that corresponds to the simulated wind, according to

$$\zeta(t) = \sum_{n=1}^N \zeta_{a_n} \cos(\omega_n t + \varepsilon) \quad (14)$$

where for each wave component  $n$ ,  $\zeta_a$  (m) is the wave amplitude,  $\omega$  (rad/s) is its frequency, and  $\varepsilon$  (rad) is a random phase angle.

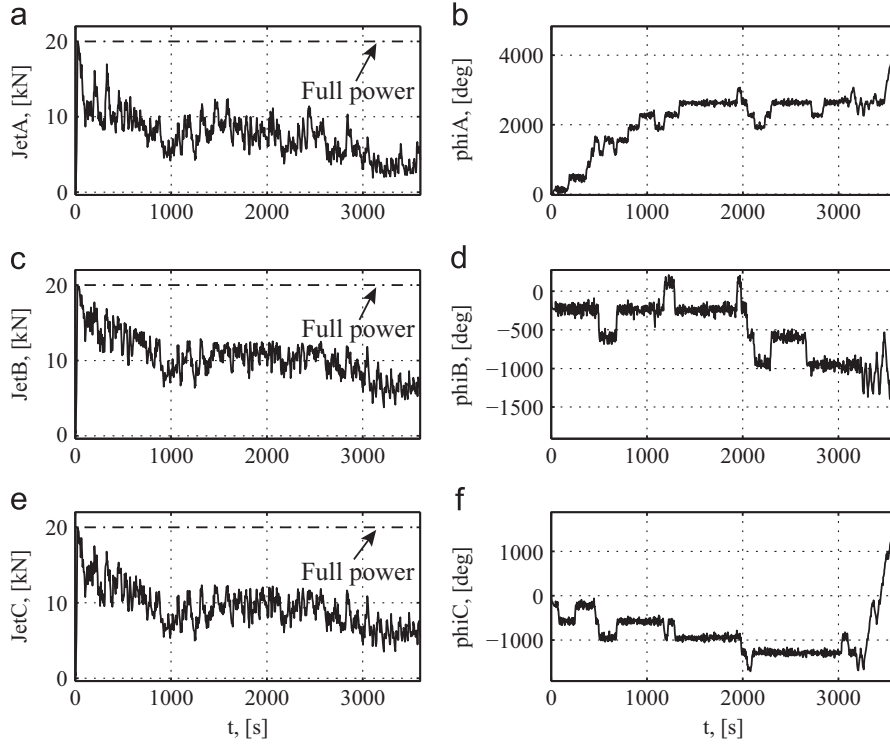


Fig. 17. (a), (c), (e) Jet thrusts, and (b), (d), (f) Jet angles.

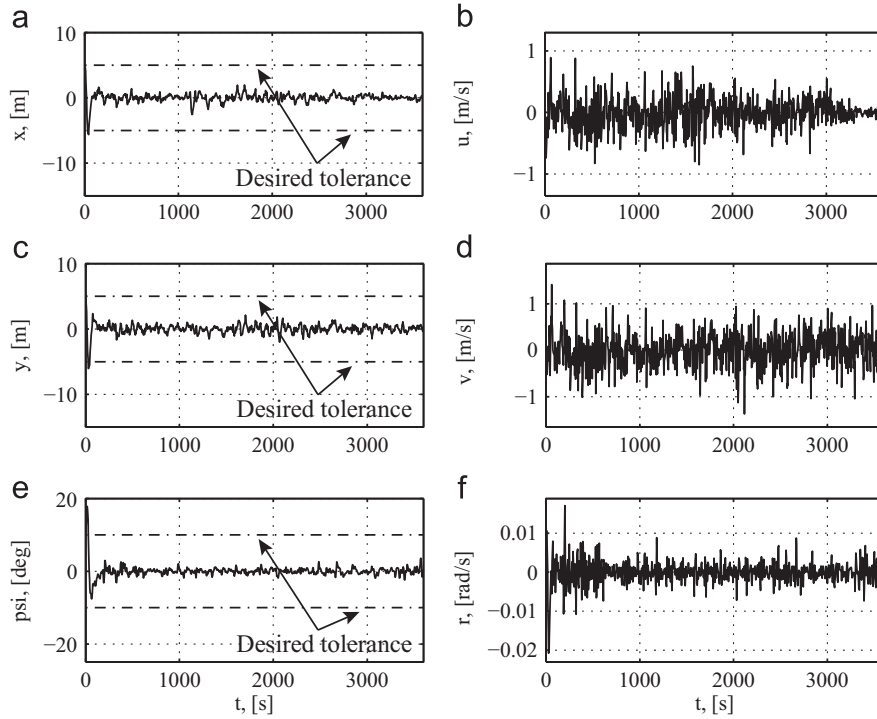


Fig. 18. (a), (c), (e) Position and orientation, and (b), (d), (f) Velocities.

To simulate the wave elevation, the Modified Two-Parameter Pierson–Moskowitz wave spectrum was used, see Fossen (1994) and Perez and Blanke (2002).

The wind induced forces (surge and sway) and moment (yaw), represented by the  ${}^B\mathbf{q}_{wind}$  in (8d), are calculated as

$$f_{x,wind} = 0.5C_X(\gamma_R)\rho V_R^2 A_T \quad (15a)$$

$$f_{y,wind} = 0.5C_Y(\gamma_R)\rho V_R^2 A_L \quad (15b)$$

$$n_{z,wind} = 0.5C_T(\gamma_R)\rho V_R^2 A_L L \quad (15c)$$

where  $C_X$  and  $C_Y$  are force coefficients and  $C_T$  is a moment coefficient (Fossen, 1994).

These coefficients are functions of the relative angle,  $\gamma_R$ , between the wind and platform direction, and are taken from tables. The symbol  $\rho$  is the density of air in  $\text{kg/m}^3$ ,  $A_T$  and  $A_L$  are the transverse and lateral projected areas in  $\text{m}^2$ , and  $L$  is the overall length of the platform in m.  $V_R$  is the relative wind speed, given in

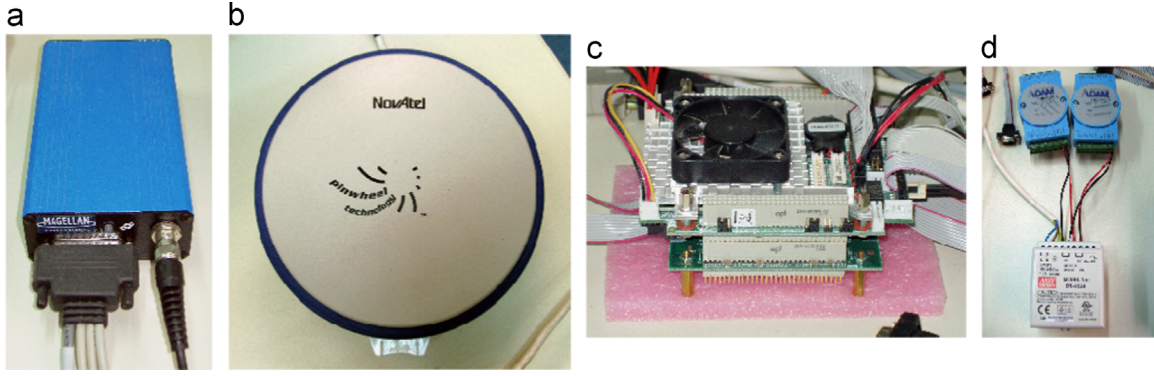


Fig. 19. (a) GPS receiver. (b) Antenna. (c) PC104 control station. (d) Analog output modules with power supply.

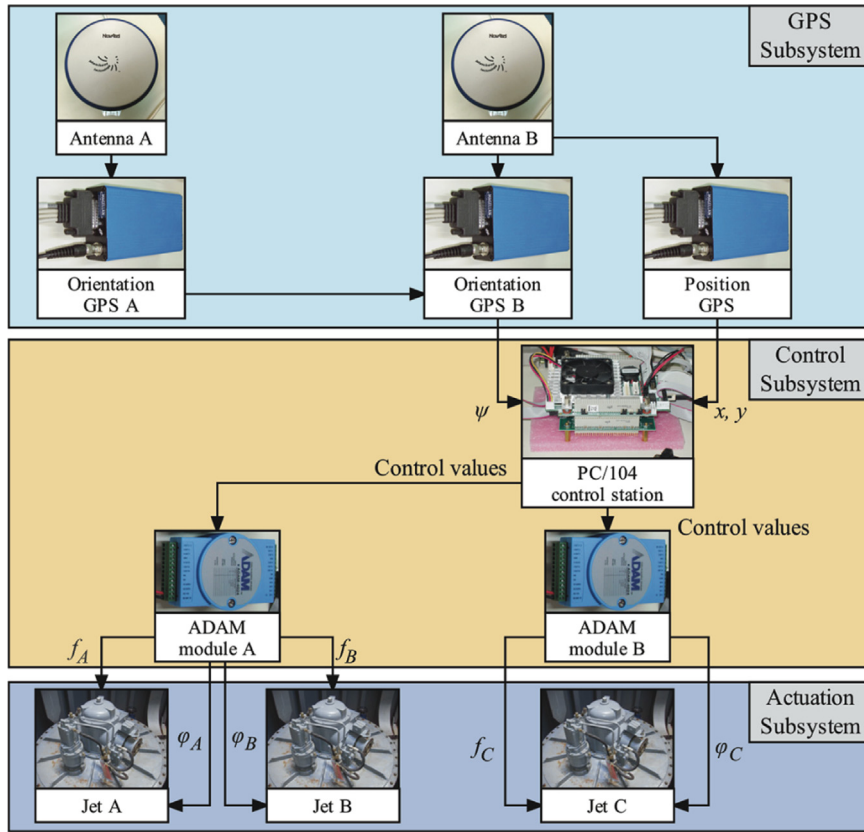


Fig. 20. Structure of the implemented system.

knots, see [Isherwood \(1972\)](#). [Figs. 9 and 10](#) show the wind forces and moment acting on the platform, and the wave forces acting on each cylinder, respectively.

#### 4. Closed loop control design and allocation

##### 4.1. Controller design

In this section we develop, following a model-based approach, a closed loop controller for dynamic positioning purposes whose control input is the vector  ${}^B\mathbf{q}_c$ . Starting from [\(8e\)](#) it holds that

$${}^B\mathbf{q}_c = \mathbf{M}^B \dot{\mathbf{v}} - {}^B\mathbf{q} - {}^B\mathbf{q}_{dist} \quad (16)$$

Using [\(1a\)](#) and its derivative,  ${}^B\dot{\mathbf{v}}$  is written as

$${}^B\dot{\mathbf{v}} = {}^I\mathbf{R}_B^{-1} ({}^I\dot{\mathbf{x}} - {}^I\dot{\mathbf{R}}_B {}^B\mathbf{v}) \quad (17)$$

and combining [\(16\)](#) and [\(17\)](#), the open-loop dynamics of the platform is described by

$${}^B\mathbf{q}_c = \mathbf{M}^I \mathbf{R}_B^{-1} {}^I\dot{\mathbf{x}} - \mathbf{M}^I \mathbf{R}_B^{-1} {}^I\dot{\mathbf{R}}_B {}^I\mathbf{R}_B^{-1} {}^I\dot{\mathbf{x}} - {}^B\mathbf{q} - {}^B\mathbf{q}_{dist} \quad (18)$$

Setting the control vector equal to

$${}^B\mathbf{q}_c = \mathbf{M}^I \mathbf{R}_B^{-1} \mathbf{f}_{fb} - \mathbf{M}^I \mathbf{R}_B^{-1} {}^I\dot{\mathbf{R}}_B {}^I\mathbf{R}_B^{-1} {}^I\dot{\mathbf{x}} - {}^B\mathbf{q} \quad (19)$$

where  $\mathbf{f}_{fb}$  is an auxiliary feedback input. This input includes proportional, derivative and integral action, and therefore can take care of constant or slow-changing and bounded environmental

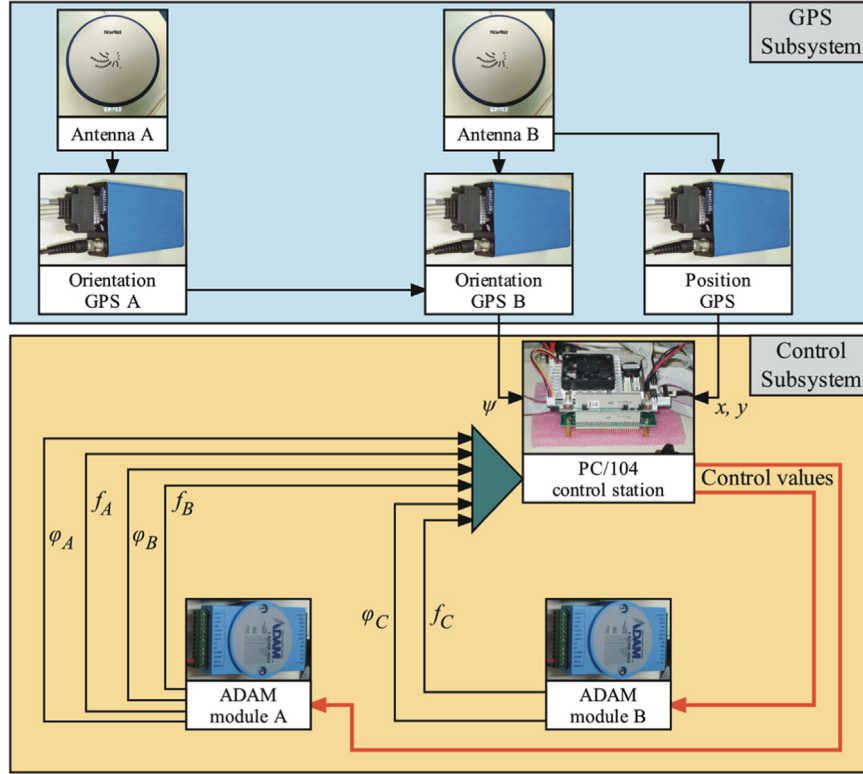


Fig. 21. HIL experimental setup.

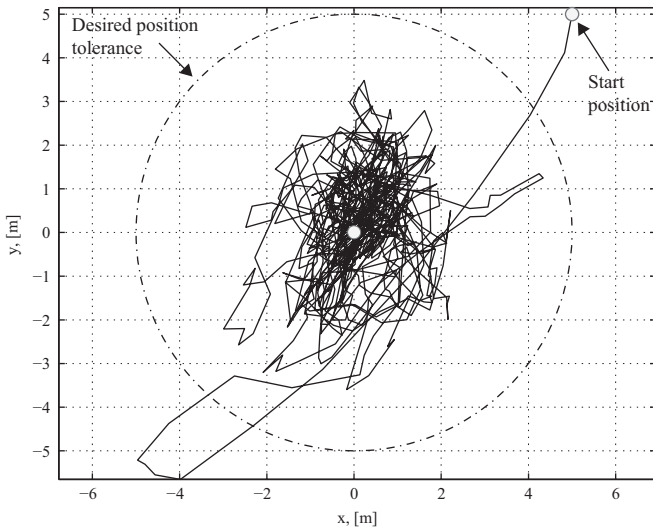


Fig. 22. Dynamic positioning with environmental disturbances (HIL exp.).

disturbances, and is given by

$$\mathbf{f}_{fb} = \ddot{\mathbf{x}}_{des} + \mathbf{K}_D \dot{\mathbf{e}} + \mathbf{K}_P \mathbf{e} + \mathbf{K}_I \int_0^t \mathbf{e} dt \quad (20a)$$

where subscript “des” denotes a reference (desired) variable and

$$\mathbf{e} = [x_{des} - x, y_{des} - y, \psi_{des} - \psi]^T \quad (20b)$$

Using the positive definite diagonal gain matrices  $\mathbf{K}_D = \text{diag}\{k_{dx}, k_{dy}, k_{d\psi}\}$ ,  $\mathbf{K}_P = \text{diag}\{k_{px}, k_{py}, k_{p\psi}\}$ , and  $\mathbf{K}_I = \text{diag}\{k_{ix}, k_{iy}, k_{i\psi}\}$ , the system closed-loop error dynamics is written as

$$\ddot{\mathbf{e}} + \mathbf{K}_D \dot{\mathbf{e}} + \mathbf{K}_P \mathbf{e} + \mathbf{K}_I \int_0^t \mathbf{e} dt = -{}^I \mathbf{R}_B \mathbf{M}^{-1} \mathbf{B} \mathbf{q}_{dist} \quad (21)$$

where the vector  ${}^I \mathbf{R}_B \mathbf{M}^{-1} \mathbf{B} \mathbf{q}_{dist}$  includes bounded disturbances. Eq. (21) corresponds to a linear and decoupled error system, allowing the selection of the control gains. To avoid oscillations, all poles of (21) are placed at the same point on the left real axis of the complex plane. The elements of the control matrices are then selected as

$$\begin{aligned} k_{px} &= k_{py} = k_{p\psi} = 3\omega_n^2 \\ k_{dx} &= k_{dy} = k_{d\psi} = 3\omega_n \\ k_{ix} &= k_{iy} = k_{i\psi} = \omega_n^3 \end{aligned} \quad (22)$$

where  $\omega_n$  represents the natural frequency of system (21) and is a design variable.

#### 4.2. Control force allocation

The control allocation scheme that has been derived is employed to distribute the forces and moments required by the closed-loop controller to the actuators such that the control objective is realized without violating thruster capabilities.

Eq. (7) describes a linear transformation between the propulsion vector  ${}^B \mathbf{f}_c$  and the control variables vector  ${}^B \mathbf{q}_c$ . To realize the control algorithm developed above, the jet thrust vector  ${}^B \mathbf{f}_c$  is calculated using (7a), according to

$${}^B \mathbf{f}_c = \mathbf{J}^+ {}^B \mathbf{q}_c + (\mathbf{I} - {}^B \mathbf{f}_c^+ {}^B \mathbf{f}_c) {}^B \mathbf{f}_{c,0} \quad (23)$$

where  $\mathbf{J}^+ = \mathbf{J}^T (\mathbf{J} \mathbf{J}^T)^{-1}$  is the pseudo-inverse of matrix  $\mathbf{J}$ . Since the system is over-actuated, an infinite number of solutions to (7a) exist. The homogenous solution in (23) can be used to achieve a desired configuration, obtaining at the same time the desired control forces. However, efficiency requirements point to jet thrust norm minimization. Therefore, only the first term of the solution of (23) is employed in computing  ${}^B \mathbf{f}_c$ .

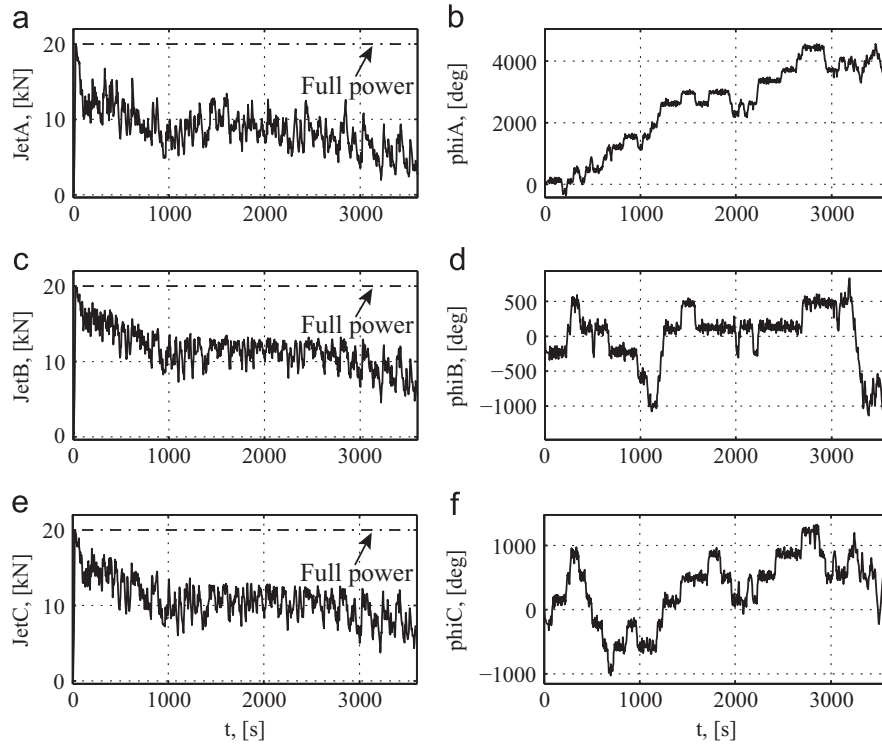


Fig. 23. (a), (c), (e) Jet thrusts, and (b), (d), (f) Jet angles (HIL exp.).

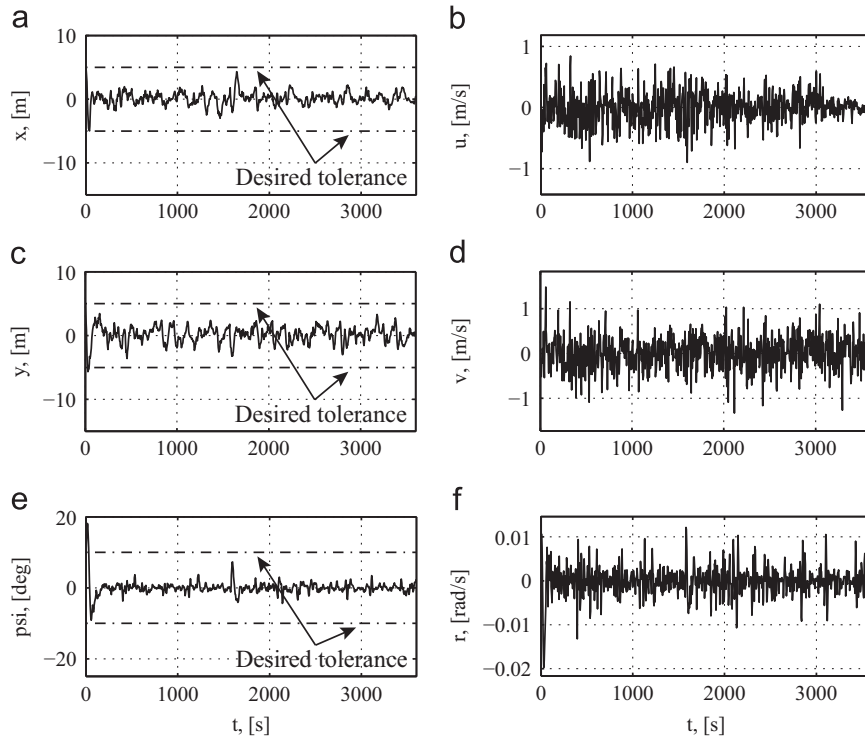


Fig. 24. (a), (c), (e) Position and orientation variables, and (b), (d), (f) Linear and angular velocities (HIL exp.).

Using (7c) and (23), we calculate the desired jet thrust and direction according to

$$f_{i,des} = \sqrt{(f_i s\varphi_i)^2 + (f_i c\varphi_i)^2}, \quad \varphi_{i,des} = a \tan 2(f_i s\varphi_i / f_i c\varphi_i) \quad (24)$$

where  $i=A, B, C$ .

## 5. Simulation results

In all examples presented in this section, the goal is to stabilize the floating platform position in a circle centered at (0,0) and of radius equal to 5 m, while keeping its orientation at  $0^\circ$ , with a tolerance equal to  $\pm 10^\circ$ , in the presence of environmental

disturbances, as described earlier. Table 1 presents the system data and initial conditions.

To choose the controller gain matrix elements, the closed-loop frequency  $\omega_n$  must be chosen. In doing this, a number of issues must be taken into account. This is addressed next.

### 5.1. Selection of $\omega_n$

The aim here is to select a value for  $\omega_n$  that results in (i) reduced fuel consumption and (ii) small positioning error. It is conjectured that smaller values of  $\omega_n$  will result in smaller controller gains and reduced propulsion, and thus in reduced fuel consumption. However, smaller values will also yield a slower system and consequently larger positioning errors. Likewise, smaller positioning errors should require increased fuel consumption and larger values of  $\omega_n$ . Therefore, the tradeoff between positioning errors and consumption must be addressed.

To study the effect of  $\omega_n$  and of the resulting controller on the response results, three sets, of 14 simulation runs each, were executed varying  $\omega_n$  from 0.02 to 0.11 rad/s with a step of 0.01 rad/s. In these, the average jet energy consumption,  $\bar{E}$ , and the average platform position error,  $\bar{e}$ , given by

$$\bar{E} = \frac{1}{3} \sum_{i=A,B,C} \int |p_i| dt, \quad \bar{e} = \frac{1}{T} \int_0^T \left( (x_{des} - x)^2 + (y_{des} - y)^2 \right)^{1/2} dt \quad (25)$$

were calculated. In (25),  $p_i$  is the input power for each jet and  $T$  is the time duration of the simulation run. In all sets, the simulation time was 900 s. The first and second sets differ by the initial platform position, under the same environmental disturbances. The second and third sets have the same start position, but differ in the parameters of the environmental disturbances. The environmental disturbances used in the simulations are marked as A and B, and are shown in Fig. 11. The magnitude and direction of the sea current and wind velocities are produced by integrating Gaussian white noise. Table 2 presents the parameters used and the related limits.

The obtained responses confirm that with larger/smaller  $\omega_n$ , the required energy, and thus the fuel consumption, is increased/reduced while the platform position errors become smaller/larger, as illustrated in Fig. 12. As shown in Fig. 12, for  $\omega_n > 0.04$  rad/s there is a constant increase of the average energy consumption without significant change in the position error. A closer look at Fig. 12 shows that for  $\omega_n > 0.07$  rad/s, there is a small increase in the position error. This is the consequence of the time delay in the rotation of the jets that results in forces with a delayed direction. Fig. 12 suggests that there is a value for  $\omega_n$  that results in reduced average energy consumption and small position error. To study this behavior, we define a normalized performance index given by

$$PI = \bar{E}/2 \times 10^5 + \bar{e}/8 \quad (26)$$

As demonstrated in Fig. 12, there is a range of values,  $0.04 < \omega_n < 0.07$  rad/s, depending on the environmental disturbances and the start position of the platform, where the position error is minimized. More specifically, it is minimized for  $\omega_n = 0.06$  rad/s in the first and second simulation sets, and for 0.05 rad/s in the third set. However, as shown in Fig. 13, the performance index, PI, is minimized for  $\omega_n = 0.04$  in all sets.

To illustrate this result, the platform motion is simulated from the same initial position (5,5) under the same environmental disturbances (see A in Fig. 11), for characteristic values of  $\omega_n$ , i.e.  $\omega_n = 0.02$  rad/s,  $\omega_n = 0.04$  rad/s,  $\omega_n = 0.07$  rad/s, and  $\omega_n = 0.11$  rad/s. The resulting platform paths and jets forces are shown in Figs. 14 and 15 respectively. Observing Fig. 14, it can be seen that in all cases the positioning goal is achieved. However, as shown in Fig. 15, the applied jet forces, and thus the consumed energy for  $\omega_n = 0.04$  rad/s (green line), is 40% less compared to that for  $\omega_n = 0.11$  rad/s (cyan line). Therefore, designing a

controller with  $\omega_n = 0.04$  rad/s offers a distinct advantage in terms of energy efficiency.

### 5.2. Controller performance

In the next simulation results, the closed-loop frequency is chosen as  $\omega_n = 0.04$  rad/s. Using (22), the controller gains are  $k_{dx} = k_{dy} = k_{d\psi} = 0.12$ ,  $k_{px} = k_{py} = k_{p\psi} = 0.0048$ , and  $k_{ix} = k_{iy} = k_{i\psi} = 0.000064$ . The simulation time is 3600 s. Fig. 16 illustrates the dynamic positioning performance of the controller against the environmental disturbances B. Fig. 17 shows the thrusts of the jets and the corresponding angles. Note that the jet thrusts and angles are relatively smooth. The platform position and orientation is depicted in Fig. 18a, c, and e while Fig. 18b, d, and f shows the linear and angular velocities. As shown in Figs. 16 and 18, the platform is stabilized within the required limits, despite the disturbances and actuators constraints.

## 6. Practical implementation

### 6.1. Hardware and software description

For the implementation of the developed control system, three GPS receivers and two antennas, see Fig. 19a and b respectively, are employed, which provide the position and orientation of the platform. Two RTK GPS receivers are connected with the antennas and give the orientation data. The position is supplied from the third receiver, also connected with one of the antennas. The receivers have an accuracy of  $\pm 1$  m with an update frequency of 5 Hz. The GPS receiver signals are transmitted to the control station via RS232 ports. The control station is a PC104 tower consisting of a cpu module and a module with four RS232 ports, see Fig. 19c. The control station is operated by the real time linux operating system Xenomai. The control algorithm and allocation scheme are coded using the C programming language. The software has as input the position and orientation of the platform and calculates according to the developed algorithms, the desired jet thrusts and angles. The use of the RTK GPSs introduces measurement noise to the position and orientation input, and in order to filter it, a Butterworth filter is used. The velocity vector is computed by differentiation. As an alternative, a Kalman filter could be employed. However, considering the slow platform dynamics and taking into account the Hardware-In-The-Loop simulation results, such a filter is not necessary. The computed control values are sent to the DAC modules ADAM (Fig. 19d), which drive the jets. The control frequency is equal to the update frequency of the GPS, i.e. 5 Hz. The implemented system, whose structure is depicted in Fig. 20, will be integrated in the platform when its construction is finished. This will allow us to try the controller in field trials.

However, to obtain an initial assessment of the developed algorithms and to validate the implemented software scheme, the GPS Subsystem, and Control Subsystem, we conducted specific preliminary Hardware-In-the-Loop (HIL) experiments.

### 6.2. Preliminary HIL experiments

The HIL experiments are conducted using the MathWorks xPC Target platform. The setup is illustrated in Fig. 21. The HIL scheme includes the actual GPS Subsystem and the Control Subsystem. The unavailable platform and the Actuation Subsystem are modeled using Matlab/Simulink according to Sections 1.3 and 1.4 respectively. The set goals were

1. to test the GPS Subsystem and Control Subsystem hardware,
2. to test our controller against unmodeled dynamics introduced by the GPS Subsystem,

3. to introduce real measurement noise, and
4. to validate the software architecture.

Using the xPC Target toolbox from MathWorks, we produced C code that implements the control algorithm and the platform and actuators models. The C code is downloaded and running in the PC104 module of the Control Subsystem. As shown in Fig. 21, the control output from the ADAM modules is fed back to the PC104 module to drive the modeled actuators and subsequently to virtually move the modeled platform. Environmental disturbances including sea current, wind, and wave forces are modeled according to Section 3.

Because no actual platform motion occurs, the GPS readings are used as measurement noise. This is achieved by subtracting from the GPS readings the position of the antenna B and the orientation of the vector connecting antennas A and B. The measurement noise is superimposed to the simulated trajectory of the platform. Next, some results using the described setup are presented. In Fig. 22, the controller dynamic positioning performance against the environmental disturbances B, described in Section 5, is illustrated. The start position and orientation of the platform are  $x_s=5$  m,  $y_s=5$  m, and  $\psi_s=10^\circ$ .

The target position and orientation of the platform are the same as in the simulation run shown in Fig. 16. Fig. 23 shows the thrusts of the jets and the corresponding angles. The platform position and orientation is depicted in Fig. 24a, c, and e, while in Fig. 24b, d, and f we see the linear and angular velocities. As shown, although the GPS sensor introduces measurement noise, the controller works as expected.

## 7. Conclusions

This paper reports the design and implementation of an autonomous dynamic positioning scheme for a new triangular floating marine platform, with real time capabilities, under realistic actuator constraints, hardware limitations, and wind, wind generated wave, and current environmental disturbances. The system is over-actuated, i.e., it has more control inputs than DOF. Hence, an appropriate control allocation scheme was developed in order to realize the control objective without violating thruster capabilities. The developed scheme is based on the norm minimization of a vector consisting of the jet thrusts. In addition, we formulated design rules that minimize the condition number of the normalized transformation matrix relating the control forces and the jets thrust of the platform. A controller, following a model-based scheme, that aims at the reduction of the fuel consumption is described and evaluated. This methodology relies on a fast, reliable, and computationally inexpensive algorithm compared to the complex, on-line, iterative ones. Simulation results and preliminary HIL experimental results including real GPS sensor measurement noise and a broad model of environmental disturbances were presented to demonstrate the performance of the controller and allocation scheme.

## Acknowledgments

This work was supported by the VERENIKI program with funding from the Hellenic Ministry of Education and Religion and the European Union.

## References

- American Petroleum Institute (API), 2000. Recommended Practice for Planning, Designing and Constructing Fixed Offshore Platforms-Working Stress Design, 21st edition.
- Braganza, D., Feemster, M., and Dawson, D., 2007. Positioning of large surface vessels using multiple tugboats. In: Proceedings the American Control Conference. ACC'07, New York, NY, pp. 912–917.
- Berge, S.P., and Fossen, T.I., 1997. Robust control allocation of over-actuated ships: experiments with a model ship. In: Proceedings of the 4th IFAC Conference on Manoeuvring and Control of Marine Craft, Brijuni, Croatia, pp. 166–171.
- Bodson, M., 2002. Evaluation of optimization methods for control allocation. *J. Guid. Control Dyn.* 25, 703–711.
- Caterpillar, 2007. 3406C Marine Propulsion, Performance no. DM6094-01, Feature code 406DM22.
- Feemster, M., Esposito, J., 2011. Comprehensive framework for tracking control and thrust allocation for a highly overactuated autonomous surface vessel. *J. Field Robot.* 28, 80–100.
- Fossen, T.I., 1994. *Guidance and Control of Ocean Vehicles*. John Wiley & Sons, UK.
- Fossen, T.I., and Johansen, T.A., 2006. A survey of control allocation methods for ships and underwater vehicles. In: Proceedings of the Mediterranean Control Conference 2006.
- Fossen, T.I., Perez, T., 2009. Kalman filtering for positioning and heading control of ships and offshore rigs. *IEEE Control Syst. Mag.* 29 (6), 32–46.
- Hawary, F.E. (Ed.), 2001. *The Ocean Engineering Handbook*. CRC Press, Boca Raton, Florida.
- Hoerner, S.F., 1965. *Fluid-Dynamic Drag*. Hoerner Publications, Bricktown, New Jersey.
- Isherwood, R.M., 1972. Wind resistance of merchant ships. *R. Inst. Nav. Archit. Trans.* 115, 327–338.
- Johansen, T.A., Fossen, T.I., Berge, S.P., 2004. Constraint nonlinear control allocation with singularity avoidance using sequential quadratic programming. *IEEE Trans. Control Syst. Technol.* TCST-12, 211–216.
- Lynch, K.M., 1999. Controllability of a planar body with unilateral thrusters. *IEEE Trans. Autom. Control* 44, 1206–1211.
- Perez, T., Blanke, M., 2002. Simulation of Ship Motion in a Seaway (Technical Report EE0237). Dept. of Electrical and Computer Engineering, The University of Newcastle, Australia.
- Repoulas, F., Vlachos, K., and Papadopoulos, E., 2008. Modeling and control of a triangular floating platform driven by rotating jets. In: Proceedings of the IEEE 16th Mediterranean Conference on Control and Automation (MED'08), Ajaccio, France, pp. 487–492.
- Schottel, 2000. SPJ 57RD, Technical Data, Ident no. HDB3007, HDB3008, HDB3009, Status 11/00.
- Sørensen, A.J., 2011. A survey of dynamic positioning control systems. *Annu. Rev. Control* 35 (1), 123–136.
- Sørdalen, O.J., 1997. Optimal thrust allocation for marine vessels. *Control Eng. Pract.* 5 (9), 1223–1231.
- Vlachos, K., and Papadopoulos, E., 2010. Control design and allocation of an over-actuated triangular floating platform. In: Proceedings of the 2010 IEEE International Conference on Robotics and Automation (ICRA'10), Anchorage, Alaska, pp. 3739–3744.
- Webster, W.C., and Sousa, J., 1999. Optimum allocation for multiple thrusters. In: Proceedings of the International Society of Offshore and Polar Engineers Conference (ISOPE'99), Brest, France.
- Wilson, J.F., 2003. *Dynamics of Offshore Structures*. John Wiley and Sons, New Jersey.